PNAS
www.pnas.org

Supplementary Information for

Rapid diffusion-state switching underlies stable cytoplasmic gradients in the *C. elegans* zygote

Youjun Wu, Bingjie Han, Younan Li, Edwin Munro, David J. Odde and Erik E. Griffin

Erik E. Griffin
Email: erik.e.griffin@dartmouth.edu

This PDF file includes:

Supplementary text
Figs. S1 to S7
Captions for movies S1 to S16
References for SI

Other supplementary materials for this manuscript include the following:

Movies S1 to S16

www.pnas.org/cgi/doi/10.1073/pnas.1722162115

Supplementary Information Text

Supplemental Methods

C. elegans strains and culturing

C. elegans strains were maintained on Nematode Growth Medium (NGM) plates with *E. coli* OP50 as a source of food, as described (1). The strains used in this study were: JH2015 GFP::PIE-1 (*unc-119(ed3) III; axIs1462[pCM4.08]*) (2); JH2078 GFP::MEX-5 (*unc-119(ed3)III; axIs1504[ppie-1::lap::mex-5::pie-13'UTR]*) (3); MG589 GFP::Utrophin (*xsSi3* II) (4), EGD359 (*unc-119(ed3) III; axIs1462[pCM4.08]; mex-5(egx7)[T186A] IV*) and EGD275 (*egxSi116 [unc-119(+); pmex-5::gfp::mex-5(F294N, F339N)]* II; *unc-119(ed3)* III) (5). All strains were maintained at 25°C. RNAi was performed using the feeding method (6) by placing L4 animals on RNAi plates for 24 hours at 25°C except for *par-1 RNAi* and *pkc-3 RNAi* which were incubated for 28 hours. GFP transgene expression levels were partially depleted by diluting GFP RNAi bacteria into control L4440, *mex-5/6*, *par-1* or *pkc-3* RNAi bacteria. For single particle tracking analysis, GFP RNAi bacteria were diluted 1:5 for GFP::MEX-5 and 1:10 for GFP::PIE-1. For smPReSS analysis, GFP RNAi bacteria were diluted 1:20.

Gene editing

The T186A mutation was introduced into the MEX-5 locus using the *dpy-10* co-CRISPR ribonucleotide complex approach (7, 8). A microinjection mix consisting of 200 ng/µL the crRNAs BH0280 (TATTCGAGACTTGTTGGAAG) and BH0281 (TGTTGGAAGAGGAGTAGACG), 1.3 µg/µL tracrRNA (Dharmacon-GE Lifesciences), 100 ng/µL of the ssODN BH0282 (GGAGATTAGTAGCACACGCACAGCTCCATTGACCTCGTCGGCCCCTCTCCCAACTAGCCTG GAATACGAGACTGTTCAGCG) and 0.67 µg/µL Cas9 protein (Dharmacon, Cat# CAS11200) were injected into the JH2015 strain.

Single particle detection and tracking

Single particle detection and tracking was based on the method described in (9, 10). Movies collected with 50 msec exposures were used to track SD particles because the signal from FD particles was sufficiently blurred that they were no longer detected as single particles. Particle detection was performed using the Kilfoil (http://people.umass. edu/kilfoil/downloads.html) implementation of the Crocker-Grier algorithm (11). Feature size, minimum intensity and integrated intensity threshold were determined empirically so that the majority of visible particles were detected. Particle trajectories were then linked within µTrack software using the Browning motion model (12). No particle splitting or merging events were allowed and a gap size of 3 frames was used to compensate for transient failures in particle detection.

For particle tracking in control (L4440 RNAi) embryos, a 5 µm wide rectangle spanning the A/P axis was divided into five equally spaced regions (regions 1-5) that were analyzed separately. For particle tracking in *mex-5/6(RNAi)*, *par-1(RNAi)*, *pkc-3(RNAi)* embryos in which PIE-1 and MEX-5 are symmetrically distributed, the entire rectangle along the A/P axis was analyzed as one region.

Estimation of short term diffusivity and appearance rate

To calculate the diffusion coefficient of slow-diffusing particles, we analyzed particles with tracks greater than 20 frames. The first five lag times of the trajectories were fit to the equation $MSD = 4D_c t^{\alpha}$ in order to calculate the short-term diffusivity D_c and the anomaly exponent α (9). To analyze the distributions of α, we first fit them into one Gaussian with mean equal to the averaged α. Because the distribution of α for GFP::MEX-5 in the anterior did not fit well with one Gaussian, we used the sum of two Gaussians with the mean of one Gaussian equal to the average α in the posterior. Violin plots were generated using an online tool (http://shiny.chemgrid.org/boxplotr/).

To determine the appearance rate of the SD particles, the number of new tracks per unit area were counted over time. Both the distribution of SD particles and the appearance rate were normalized to the region of low concentration (the posterior for MEX-5 and the anterior for PIE-1). All tracks longer than 2 frames were used for appearance rate and distribution analyses. Note that we cannot directly compare appearance rates between embryos due to variability in the number of GFP molecules and in illumination.

Simulated trajectories of pure Brownian motion

For each data set used to estimate short term diffusivities, we simulated trajectories assuming pure Brownian motion using track lengths and total number of trajectories equal to those of the experimental tracks. At each step in the simulation, we allowed the particles to be displaced in both the x and y direction following a Gaussian probability density function with a standard deviation given by $\sqrt{2 * D * t}$, where t was the interval between frames of the experimental data (50 msec), D was randomly chosen from a normal distribution with mean equal to the observed mean value and standard deviation equal to 1/3 of the mean. We then followed the same procedure to estimate the short-term diffusivity and anomalous diffusion exponent as we did for the experimental data.

smPReSS

Imaging for smPReSS analysis was performed using 50% laser power and 50 msec exposures. Five initial frames were taken at 5 second intervals to establish the initial steady-state particle number. Next, continuous imaging was performed for 300 frames, at which point the new quasi-steady state was reached. After a 45 second recovery interval with no imaging, five additional frames were taken at 5 second intervals to determine the final steady state particle number. Only embryos in which the final steady state recovered to >80% of the initial steady state were analyzed. A 5 μm wide rectangle spanning the A/P axis was analyzed and particles were counted using the single particle detection approach described above. The number of particles in each frame was plotted over time and the bleaching portion was fit to the equation $X=(X_{SS}-X_{SS}')*\exp[-(k_{ph}+ k_{S\rightarrow F})t]+X_{SS}'$ (equation 1), where X is the number of slow-diffusing particles in each frame, t is time in second, X_{SS} is the number of slow-diffusing particles at the initial steady state, X_{SS}' is the number of particles at the new quasi-steady state, k_{ph} and $k_{S\rightarrow F}$ are pseudo-first-order rate constants of bleaching and dissociation (9). We used non-linear least squares to fit equation (1) in Matlab (version R2016b, MathWorks), with X_{SS} equal to the average number of particles in the first five frames before bleaching, to get an estimate for $k_{ph}+ k_{S\rightarrow F}$ and X_{SS}'. The estimate of X_{SS}' is close to the average number of slow-diffusing particles at the end of the decay, suggesting that a new quasi-steady state was reached. We then used $f = k_{S\rightarrow F} /(k_{ph}+ k_{S\rightarrow F})$ to estimate $k_{S\rightarrow F}$, where f approximates to X_{SS}'/X_{SS} if the depletion of the cytoplasmic pool of GFP-labeled molecules is negligible. t-tests were performed for $k_{S\rightarrow F}$ in GraphPad Prism 6 (GraphPad Software, La Jolla, CA) to determine statistical significance.

Simulations of gradient formation

Parameters common to the MEX-5 and PIE-1 simulations:

The MEX-5 and PIE-1 models were derived from a previous 1D MEX-5 reaction-diffusion model (13). Molecules diffuse along a one-dimensional A/P axis in either the fast-diffusing (FD) or slow-diffusing (SD) state and switch between the FD and SD states with kinetics that vary along the A/P axis. The change in the concentration of FD and SD molecules over time is described by the following differential equations:

$$\frac{\partial [FD]}{\partial t} = k_{\mathrm{S}\rightarrow\mathrm{F}}\,[SD] - k_{\mathrm{F}\rightarrow\mathrm{S}}\,[FD] + D_{c(FD)}\frac{\partial^2 [FD]}{\partial x^2} \quad (2)$$

$$\frac{\partial [SD]}{\partial t} = -k_{\mathrm{S}\rightarrow\mathrm{F}}\,[SD] + k_{\mathrm{F}\rightarrow\mathrm{S}}\,[FD] + D_{c(SD)}\frac{\partial^2 [SD]}{\partial x^2} \quad (3)$$

where t is time in seconds. [*FD*] and [*SD*] are the local concentrations of FD molecules and SD molecules. $D_{C(FD)}$ and $D_{C(SD)}$ are the diffusion coefficients of FD and SD molecules, $k_{S\rightarrow F}$ is the rate constant of a molecule transitioning from the SD to FD state, $k_{F\rightarrow S}$ is the rate constant of a molecule transitioning from the FD to SD state. $D_{C(FD)}$ is set to 5 $\mu m^2/s$ based on previous FCS analysis of GFP::MEX-5 (13) and $D_{C(SD)}$ is set to 0.1 $\mu m^2/s$ based on single particle tracking analysis in this paper. x is the spatial coordinate ranging from 0 to L of a one-dimensional Cartesian coordinate system where 0 is the anterior end and L is the posterior end. L equals 32 μm for the near-cortex simulation and 50 μm for the midplane simulation. For 50 μm simulations, we assume that $k_{S\rightarrow F}$ and $k_{F\rightarrow S}$ at $9\leq x\leq 41$ in the midplane are equivalent to the corresponding regions on the cortex ($0\leq x\leq 32$), and we set $k_{S\rightarrow F}$ and $k_{F\rightarrow S}$ constant from $0\leq x\leq 9$ and $41\leq x\leq 50$. Other parameters are kept the same in this simulation.

At the boundaries x = 0 and x = L, we impose no flux conditions for both FD molecules and SD molecules, so that

$$\frac{\partial [FD]}{\partial x}|_{x=0} = \frac{\partial [FD]}{\partial x}|_{x=L} = \frac{\partial [SD]}{\partial x}|_{x=0} = \frac{\partial [SD]}{\partial x}|_{x=L} = 0$$

The initial condition is that 0.7μM FD and 0.3μM SD molecules are uniformly distributed along the A/P axis. We note that the final steady-state condition is not sensitive to changes in the initial concentrations of FD and SD molecules.

Using Matlab pdepe Solver, equations (2) and (3) can be solved for [*FD*], [*SD*] and [Total], which equals ([*FD*]+[*SD*]), at specific values for x and t.

Parameters specific to the MEX-5 model:

$k_{S\rightarrow F}$. To set $k_{S\rightarrow F}$ for MEX-5 along the A/P axis, we assume that $k_{S\rightarrow F}$ increases linearly along the A/P-axis starting at x = 0 (i.e., the anterior end of the embryo), with $k_{S\rightarrow F}=0.12$ at x=3.2 (the middle point of region 1) and $k_{S\rightarrow F}=0.22\ s^{-1}$ at x=28.8 (the middle point of region 5) based on our smPReSS analysis.

$k_{F\rightarrow S}$. At steady state, $[FD] * k_{\mathrm{F}\rightarrow\mathrm{S}} \approx [SD] * k_{\mathrm{S}\rightarrow\mathrm{F}}$, from which we have:

$$k_{\mathrm{F}\rightarrow\mathrm{S}} \approx k_{\mathrm{S}\rightarrow\mathrm{F}}\,\frac{[SD]}{[FD]} \quad (4)$$

In order to estimate $k_{F\rightarrow S}$, we first estimated the relative concentrations of MEX-5 FD and SD molecules in the anterior and posterior cytoplasm. The mean total MEX-5 concentration in anterior (region 1) is 2.66X higher than in the posterior (region 5). Therefore,

$$([FD_{ant}] + [SD_{ant}])/([FD_{post}] + [SD_{post}]) = 2.66 \text{ (Figure 1C)}$$

Assuming that

$$[FD_{ant}] \approx [FD_{post}] \text{ and}$$
$$[SD_{ant}]/5.28 = [SD_{post}] \text{ (Figure 1E)}$$

then

$$[SD_{ant}]/[FD_{ant}] = 3.3 \text{ and}$$
$$[SD_{post}]/[FD_{post}] = 0.63$$

Using equation (4), we can estimate that for MEX-5, $k_{F\rightarrow S\,(ant)} = 0.40\ s^{-1}$ and $k_{F\rightarrow S\,(post)} = 0.14\ s^{-1}$. These initial estimates for $k_{F\rightarrow S}$ were tested in our MEX-5 gradient simulation, and revised slightly to account for the weak gradient in the distribution of FD molecules and to match the relative differences in SD appearance rate in the five regions along the A/P axis (derived from Figure 2A).

Parameters specific to the PIE-1 model:

$k_{S\rightarrow F}$. To set $k_{S\rightarrow F}$ for PIE-1 along the A/P axis, we assume that $k_{S\rightarrow F}$ reflects the distribution of MEX-5 SD particles so that $k_{S\rightarrow F}$ remains constant ($0.20\ s^{-1}$) at $0 \leq x \leq 9.6$ (the middle point of region 2) and then decreases linearly toward posterior with $k_{S\rightarrow F}=0.13\ s^{-1}$ at $x=28.8$ (the middle point of region 5), based on our smPReSS analysis.

$k_{F\rightarrow S}$. We estimated $k_{F\rightarrow S}$ using a similar approach as described above for MEX-5. For PIE-1, the mean total PIE-1 concentration in posterior (region 5) is 3.76X higher than in the Anterior (region 1). Therefore,

$$([FD_{post}] + [SD_{post}])/([FD_{ant}] + [SD_{ant}]) = 3.76 \text{ (Figure 1C)}$$

Assuming that

$$[FD_{ant}] \approx [FD_{post}] \text{ and}$$
$$[SD_{post}]/9.44 = [SD_{ant}] \text{ (Figure 1E)}$$

then

$$[SD_{ant}]/[FD_{ant}] = 0.49 \text{ and}$$
$$[SD_{post}]/[FD_{post}] = 4.58.$$

Using equation (4), we can estimate that for PIE-1, $k_{F\rightarrow S\,(ant)} = 0.10$ and $k_{F\rightarrow S\,(post)} = 0.60$. These initial estimates for $k_{F\rightarrow S}$ were tested in simulations and revised slightly to account for the weak gradient in the

distribution of FD molecules and to match the relative differences in SD appearance rate in the five regions along the A/P axis (derived from Figure 3A).

To test the sensitivity of the initial MEX-5 and PIE-1 models to changes in the diffusion coefficient of the FD and SD particles, we changed $D_{C(FD)}$ and $D_{C(SD)}$ accordingly and kept all the other parameters the same. To test the individual contributions of $k_{S\rightarrow F}$ and $k_{F\rightarrow S}$ to the amplitude of concentration gradient, we set one parameter constant along the A/P axis while keeping the other one unchanged. For comparison purposes, we choose the average of the original $k_{S\rightarrow F}$ or $k_{F\rightarrow S}$ as the constant value. To test the sensitivity of the models to the absolute values of $k_{S\rightarrow F}$ and $k_{F\rightarrow S}$, we systematically increased or decreased $k_{S\rightarrow F}$ and/or $k_{F\rightarrow S}$ while maintaining the relative change in kinetics along the A/P axis. All sensitivity tests were done in the 32 μm model.

To test the effects of embryo length on the dynamics of gradient formation (Figure 5N and 5O), we varied the length of the simulation axis L while keeping the values for $k_{S\rightarrow F}$ and $k_{F\rightarrow S}$ at the boundaries constant. Therefore, the slope at which these values change along the embryo axis varies inversely with respect to the L.

FRAP simulations

FRAP simulations were conducted using a cylindrical coordinate system with a radius of 20 μm, which is roughly the average distance of the FRAP (bleach) ROI to the boundary of the cell in our FRAP experiments. The simulated FRAP ROI was a cylindrical region with a radius of 2 μm positioned at the center of the domain (Fig. S5A). The simulations assume that all recovery is radial and symmetric around the z axis. To plot recovery within the circular ROI (Figs. 4I-L, 5G-I), intensity values at various radii were weighted to account for the cylindrical geometry.

Two component simulations: For each FRAP simulation, we first considered a two component model based on the following equations:

$$\frac{\partial [FD]}{\partial t} = k_{\mathrm{S}\rightarrow\mathrm{F}}\,[SD] - k_{\mathrm{F}\rightarrow\mathrm{S}}\,[FD] + D_{c(FD)}\,\frac{1}{r}\frac{\partial}{\partial r}\left(r\frac{\partial [FD]}{\partial r}\right) \quad (5)$$

$$\frac{\partial [SD]}{\partial t} = -k_{\mathrm{S}\rightarrow\mathrm{F}}\,[SD] + k_{\mathrm{F}\rightarrow\mathrm{S}}\,[FD] + D_{c(SD)}\,\frac{1}{r}\frac{\partial}{\partial r}\left(r\frac{\partial [SD]}{\partial r}\right) \quad (6)$$

where r is the spatial coordinate ranging from 0 to 20 μm of the cylindical coordinate system where 0 μm is the center of the domain and 20 μm is the domain boundary. FRAP recovery curves were simulated for the anterior and posterior cytoplasm separately. No flux boundary conditions were imposed at $r = 0$ and $r = 20$ μm for both FD and SD, so that

$$\frac{\partial [FD]}{\partial r}|_{r=0} = \frac{\partial [FD]}{\partial r}|_{r=L} = \frac{\partial [SD]}{\partial r}|_{r=0} = \frac{\partial [SD]}{\partial r}|_{r=L} = 0$$

Prior to simulated photobleaching, the concentrations of FD particles and SD particles were uniform and at steady state with a total concentration ([FD]+[SD]) = 1μM. At steady state: $[FD] * k_{\mathrm{F}\rightarrow\mathrm{S}} \approx [SD] * k_{\mathrm{S}\rightarrow\mathrm{F}}$, from which we can derive the fractions of FD and SD particles:

$$f_F = \frac{k_{\mathrm{S}\to\mathrm{F}}}{k_{\mathrm{F}\to\mathrm{S}} + k_{\mathrm{S}\to\mathrm{F}}}$$
$$f_S = \frac{k_{\mathrm{F}\to\mathrm{S}}}{k_{\mathrm{F}\to\mathrm{S}} + k_{\mathrm{S}\to\mathrm{F}}}$$

To mimic photobleaching, the concentration of FD and SD particles were set to 0 within a 2 μm radius circular region ($0 \le r \le 2$) using the Heavyside step function in Matlab, which is the initial condition at time = 0. Using Matlab pdepe Solver, [*FD*] and [*SD*] were solved from equation (5) and (6) at specific values for *r* and *t*, which was used to calculate the total concentration within the bleach domain over time.

Three component simulations:

The simulated percent recovery using the two state model was higher than the observed percent recovery for GFP::MEX-5 in the anterior and posterior and GFP::PIE-1 in the posterior. Therefore, we next considered three component models that were identical to the two component model except that they included Very Slow Diffusing particles (VSD; D_c = 0.01 μm^2/sec) that exchanges relatively slowly. Molecules were allowed to transition between FD and SD, and between FD and VSD, i.e., $FD \leftrightarrows SD, FD \leftrightarrows VSD,$ from which we have:

$$\frac{\partial[FD]}{\partial t} = k_{\mathrm{S}\to\mathrm{F}}\,[SD] + k_{\mathrm{VS}\to\mathrm{F}}\,[VSD] - k_{\mathrm{F}\to\mathrm{S}}\,[FD] - k_{\mathrm{F}\to\mathrm{VS}}\,[FD] + D_{c(FD)}\,\frac{1}{r}\frac{\partial}{\partial r}\left(r\frac{\partial[FD]}{\partial r}\right)$$
$$\frac{\partial[SD]}{\partial t} = -k_{\mathrm{S}\to\mathrm{F}}\,[SD] + k_{\mathrm{F}\to\mathrm{S}}\,[FD] + D_{c(SD)}\,\frac{1}{r}\frac{\partial}{\partial r}\left(r\frac{\partial[SD]}{\partial r}\right)$$
$$\frac{\partial[VSD]}{\partial t} = -k_{\mathrm{VS}\to\mathrm{F}}\,[VSD] + k_{\mathrm{F}\to\mathrm{VS}}\,[FD] + D_{c(VSD)}\,\frac{1}{r}\frac{\partial}{\partial r}\left(r\frac{\partial[VSD]}{\partial r}\right)$$

No flux boundary conditions were imposed at $r = 0$ and $r = 20$ μm for all three components, so that

$$\frac{\partial[FD]}{\partial r}\Big|_{r=0} = \frac{\partial[FD]}{\partial r}\Big|_{r=L} = \frac{\partial[SD]}{\partial r}\Big|_{r=0} = \frac{\partial[SD]}{\partial r}\Big|_{r=L} = \frac{\partial[VSD]}{\partial r}\Big|_{r=0} = \frac{\partial[VSD]}{\partial r}\Big|_{r=L} = 0$$

At steady state,

$$[FD] * k_{\mathrm{F}\to\mathrm{S}} \approx [SD] * k_{\mathrm{S}\to\mathrm{F}}$$
$$[FD] * k_{\mathrm{F}\to\mathrm{VS}} \approx [VSD] * k_{\mathrm{VS}\to\mathrm{F}}$$

from which we can derive the fractions of FD, SD and VSD molecules:

$$f_F = \frac{1}{\frac{k_{\mathrm{F}\to\mathrm{S}}}{k_{\mathrm{S}\to\mathrm{F}}} + 1 + \frac{k_{\mathrm{F}\to\mathrm{VS}}}{k_{\mathrm{VS}\to\mathrm{F}}}}$$
$$f_S = \frac{k_{\mathrm{F}\to\mathrm{S}}}{k_{\mathrm{S}\to\mathrm{F}}} * f_F$$
$$f_{VS} = \frac{k_{\mathrm{F}\to\mathrm{VS}}}{k_{\mathrm{VS}\to\mathrm{F}}} * f_F$$

Similar procedures were performed to get the initial condition as conducted in the two component model.

We assume that the kinetics of $FD \leftrightharpoons VSD$ should be significantly lower than $FD \leftrightharpoons SD$. From our single particle tracking analyses of GFP::MEX-5 in the anterior, we estimate that ~25% of particles tracked have a D_c = 0.01 μm^2/sec. Therefore, we constrained the ratio of [SD]:[VSD] to be ~3:1. The concentration of VSD particles was varied by changing $k_{F\rightarrow VS}$ and $k_{VS\rightarrow F}$ until the percent recovery was similar to the observed percent recovery.

Three component MEX-5 gradient simulation

To test if the VSD component has a major effect in gradient formation (Figure 4M), we incorporated it into the base simulation of MEX-5 gradient formation. We used the values of $k_{F\rightarrow VS}$ and $k_{VS\rightarrow F}$ listed in Figs. 4J and 4L at the middle point of anterior (x = 3.2) and posterior (x = 28.8), and we allowed $k_{F\rightarrow VS}$ and $k_{VS\rightarrow F}$ to vary along the A/P axis linearly. The initial conditions and boundary conditions are similar to the two component base simulation. Based on the following equations, we can solve [SD], [FD], [VSD] at different times and different x using Matlab pdepe Solver.

$$\frac{\partial [FD]}{\partial t} = k_{\mathrm{S}\rightarrow\mathrm{F}}\,[SD] + k_{\mathrm{VS}\rightarrow\mathrm{F}}\,[VSD] - k_{\mathrm{F}\rightarrow\mathrm{S}}\,[FD] - k_{\mathrm{F}\rightarrow\mathrm{VS}}\,[FD] + D_{c(FD)}\frac{\partial^2 [FD]}{\partial x^2}$$

$$\frac{\partial [SD]}{\partial t} = -k_{\mathrm{S}\rightarrow\mathrm{F}}\,[SD] + k_{\mathrm{F}\rightarrow\mathrm{S}}\,[FD] + D_{c(SD)}\frac{\partial^2 [SD]}{\partial x^2}$$

$$\frac{\partial [VSD]}{\partial t} = -k_{\mathrm{VS}\rightarrow\mathrm{F}}\,[VSD] + k_{\mathrm{F}\rightarrow\mathrm{VS}}\,[FD] + D_{c(VSD)}\frac{\partial^2 [VSD]}{\partial x^2}$$

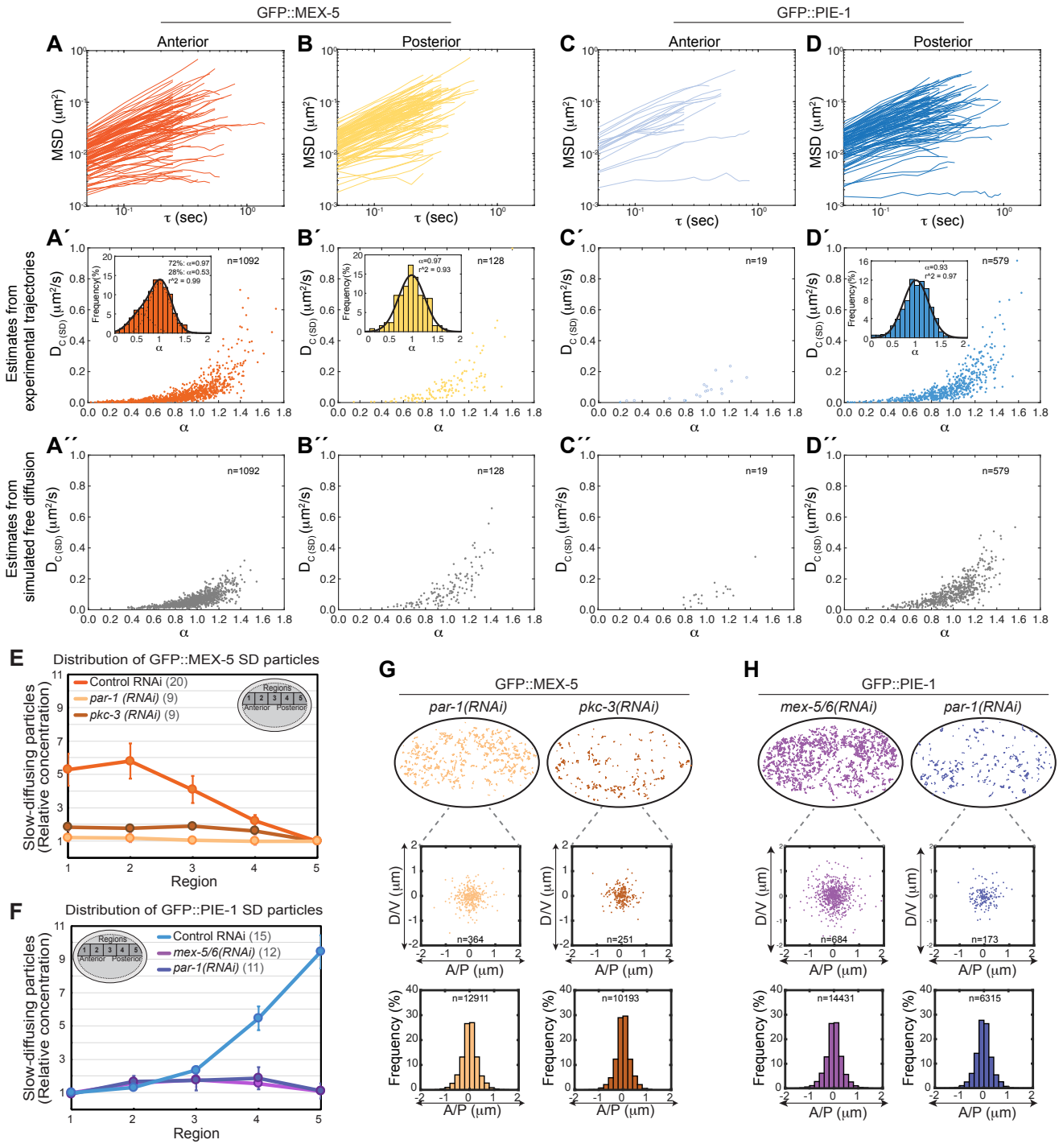

Fig. S1. Analysis of GFP::MEX-5 and GFP::PIE-1 SD particle dynamics. Related to Figure 1. **A-D.** Mean squared displacement (MSD) versus tau for individual SD particle trajectories. Only a subset of all trajectories are presented here. **A´-D´.** D_c and α values derived from fitting all trajectories including the ones in panels A-D. Inset: Histogram of α. No histogram is plotted for GFP::PIE-1 in the anterior due to limited number of trajectories. The distribution of α can be fit well with the sum of two Gaussians with means equal to 0.97 and 0.53 for GFP::MEX-5 in the anterior, and with one Gaussian for GFP::MEX-5 in the posterior and GFP::PIE-1 in the posterior. R^2 indicates how well the distribution is fit by the Gaussians. n = the number of trajectories used for the estimate. **A´´-D´´.** D_c and α values derived from fitting simulated trajectories undergoing Brownian diffusion with $D_c = 0.058 \pm 0.019$ μm²/sec for GFP::MEX-5 in the anterior, 0.11 ± 0.037 μm²/sec in the

posterior, 0.08 ± 0.027 μm^2/sec for GFP::PIE-1 in the anterior and 0.10 ± 0.033 μm^2/sec in the posterior. n = the number of trajectories used for the estimate. Note that the overall heterogeneity in estimated of D_c and α result from fitting short trajectories since the simulated trajectories also result in wide ranges of estimated D_c and α. **E, F.** Relative concentration of GFP::MEX-5 (E) and GFP::PIE-1 (F) SD particles in embryos of the indicated genotype (as in Fig. 1E). The same control RNAi data are also presented in Figure 1E. **G, H.** Tracks of GFP::MEX-5 and GFP::PIE-1 SD particles in embryos of the indicated genotype as in Figures 1F and 1G, except that tracks are from region 3. n = the number of track displacements plotted.

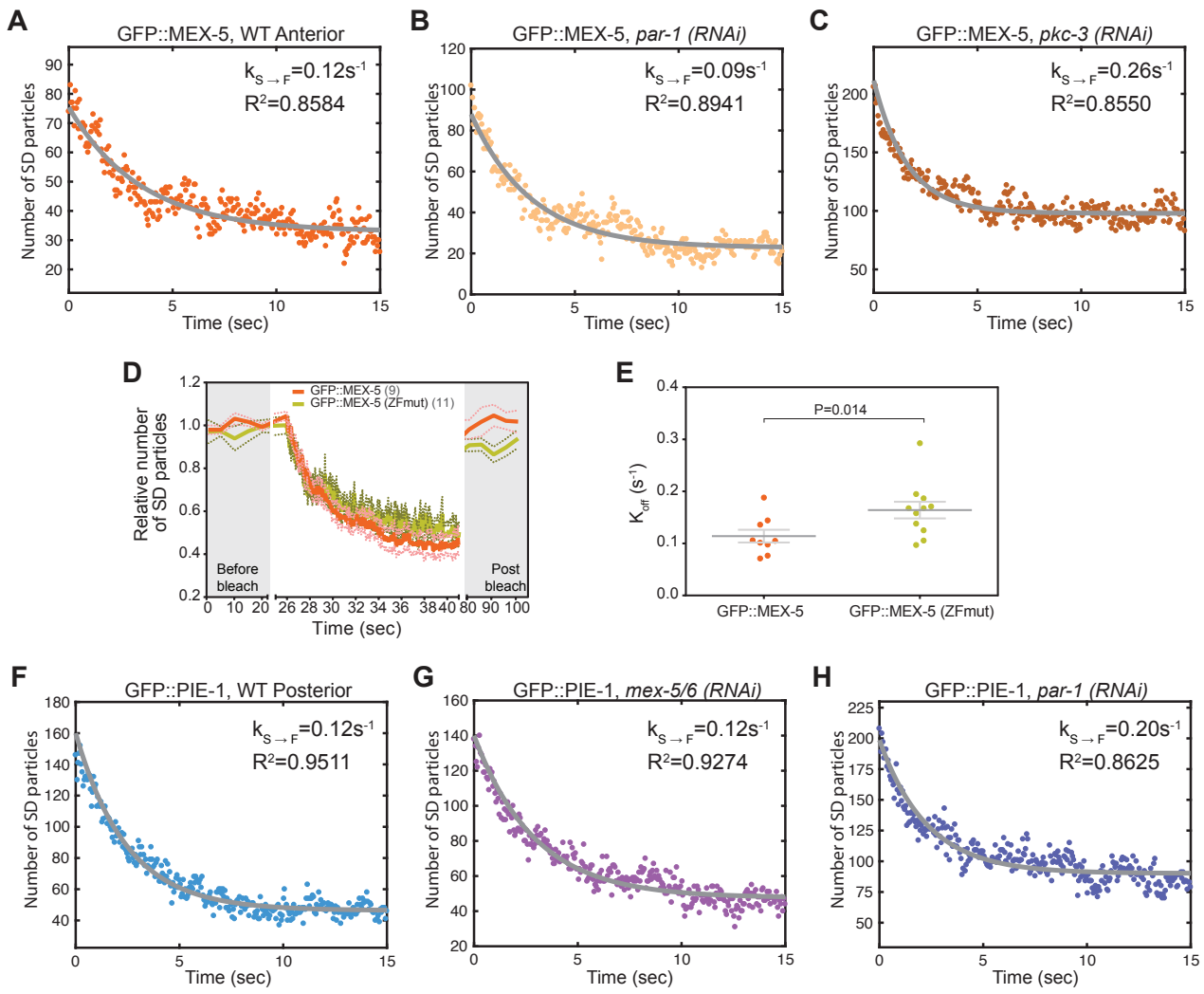

Fig. S2. smPReSS analysis of GFP::MEX-5 and GFP::PIE-1. Related to Figures 2 and 3. **A-C, F-H.** Individual representative smPReSS curves of GFP::MEX-5 and GFP::PIE-1 SD particles in embryos of the indicated genotypes. The $k_{S\rightarrow F}$ and curve fit (R^2) for the individual curves are indicated. **D.** smPReSS curves of GFP::MEX-5 and GFP::MEX-5(ZFmut) in the anterior cytoplasm. The number of SD particles is normalized to the mean number of prebleach particles for each embryo and then averaged among the indicated number of embryos. Dotted curves indicate the SEM. **E.** Apparent $k_{S\rightarrow F}$ estimated from the smPReSS curves in panel D for GFP::MEX-5 and GFP::MEX-5(ZFmut).

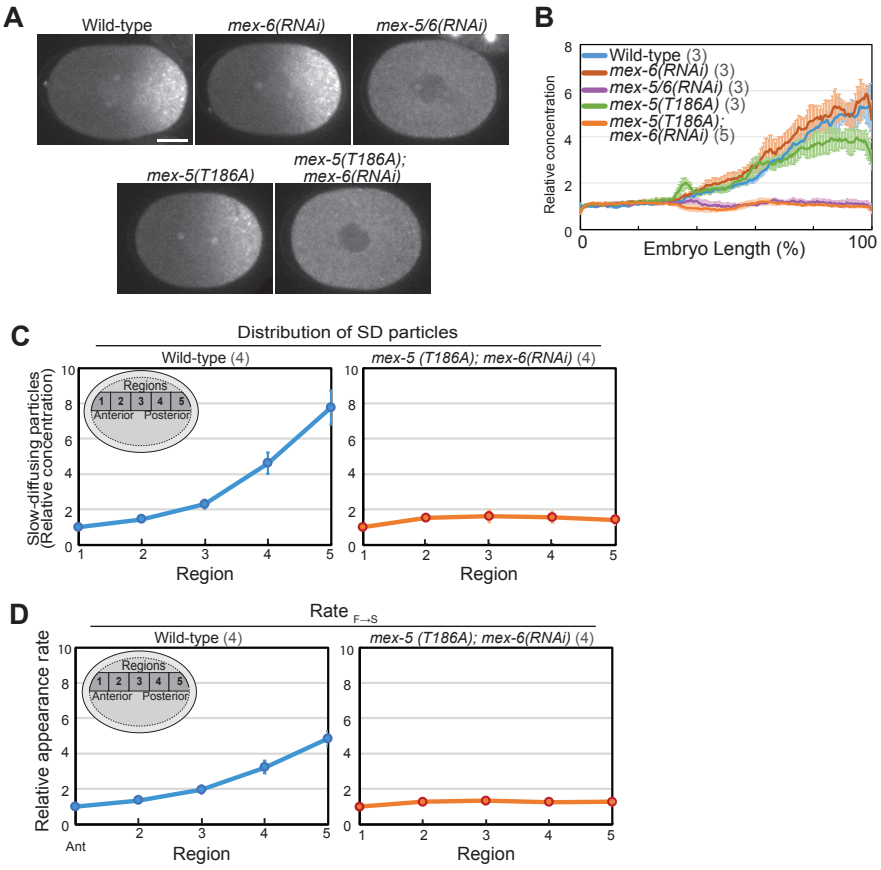

Fig. S3. GFP::PIE-1 dynamics in *mex-5(T186A);mex-6(RNAi)* embryos. **A.** Images of GFP::PIE-1 in NEBD embryos of the indicated genotype. Anterior is to the left and posterior is to the right. Note that *mex-6(RNAi)* does not affect MEX-5 expression levels (5). Scale bar = 10 μm. **B.** Quantification of the GFP::PIE-1 gradient in NEBD embryos of the indicated genotype. Gradients are normalized to GFP::PIE-1 concentration at the anterior pole. The number of embryos is indicated following the genotype. **C.** Distribution of SD GFP::PIE-1 particles averaged from the indicated number of wild-type and *mex-5(T186A);mex-6(RNAi)* embryos. **D.** Quantification of GFP::PIE-1 $Rate_{F \rightarrow S}$ in wild-type and *mex-5(T186A);mex-6(RNAi)* embryos.

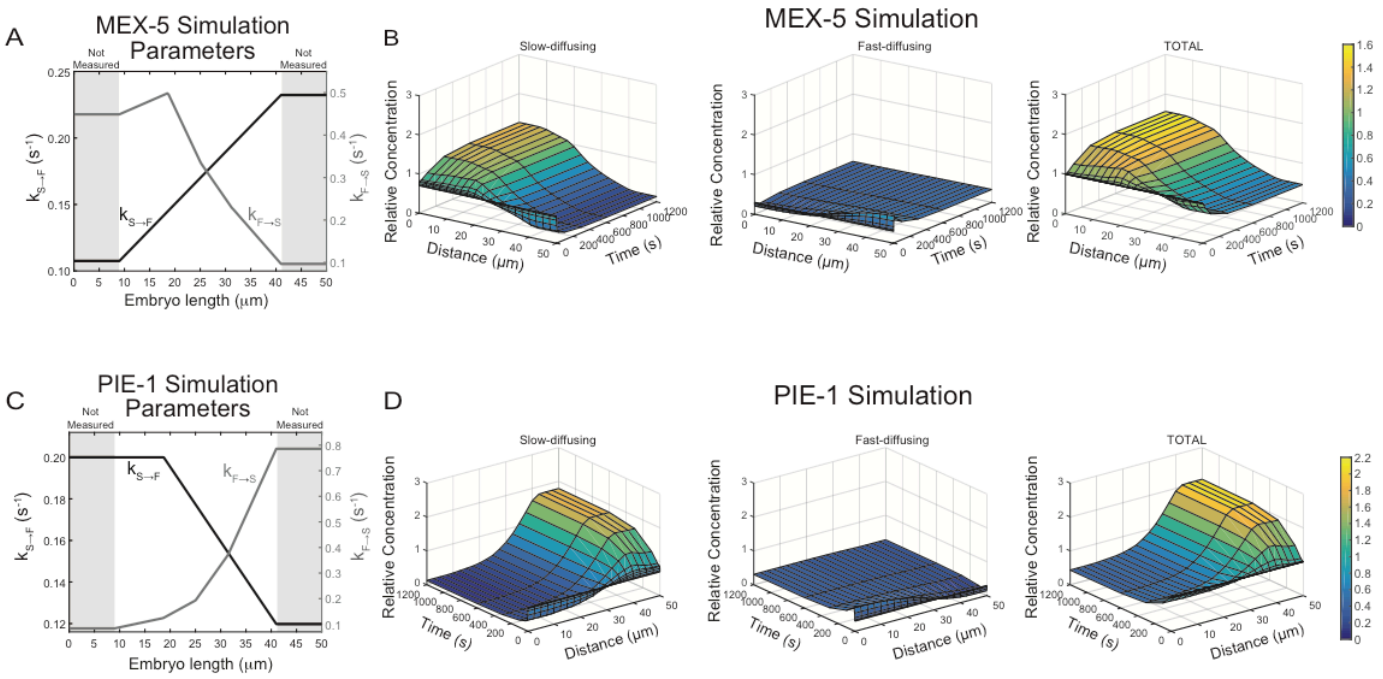

Fig. S4. Simulation of MEX-5 and PIE-1 differential diffusion with 50 μm length scales. Related to Figures 4 and 5. **A, C.** Schematic of the $k_{S\rightarrow F}$ and $k_{F\rightarrow S}$ parameters used in the MEX-5 (panel A) and PIE-1 (panel C) simulations. The values near the anterior and posterior boundaries (indicated in grey) were not experimentally measured, and are assumed to be equivalent to the most anterior and posterior values measured. **B, D.** The relative concentration of FD, SD and Total MEX-5 (panel B) and PIE-1 (panel D) over time. Note that the MEX-5 and PIE-1 gradients reach steady state within ~6 minutes.

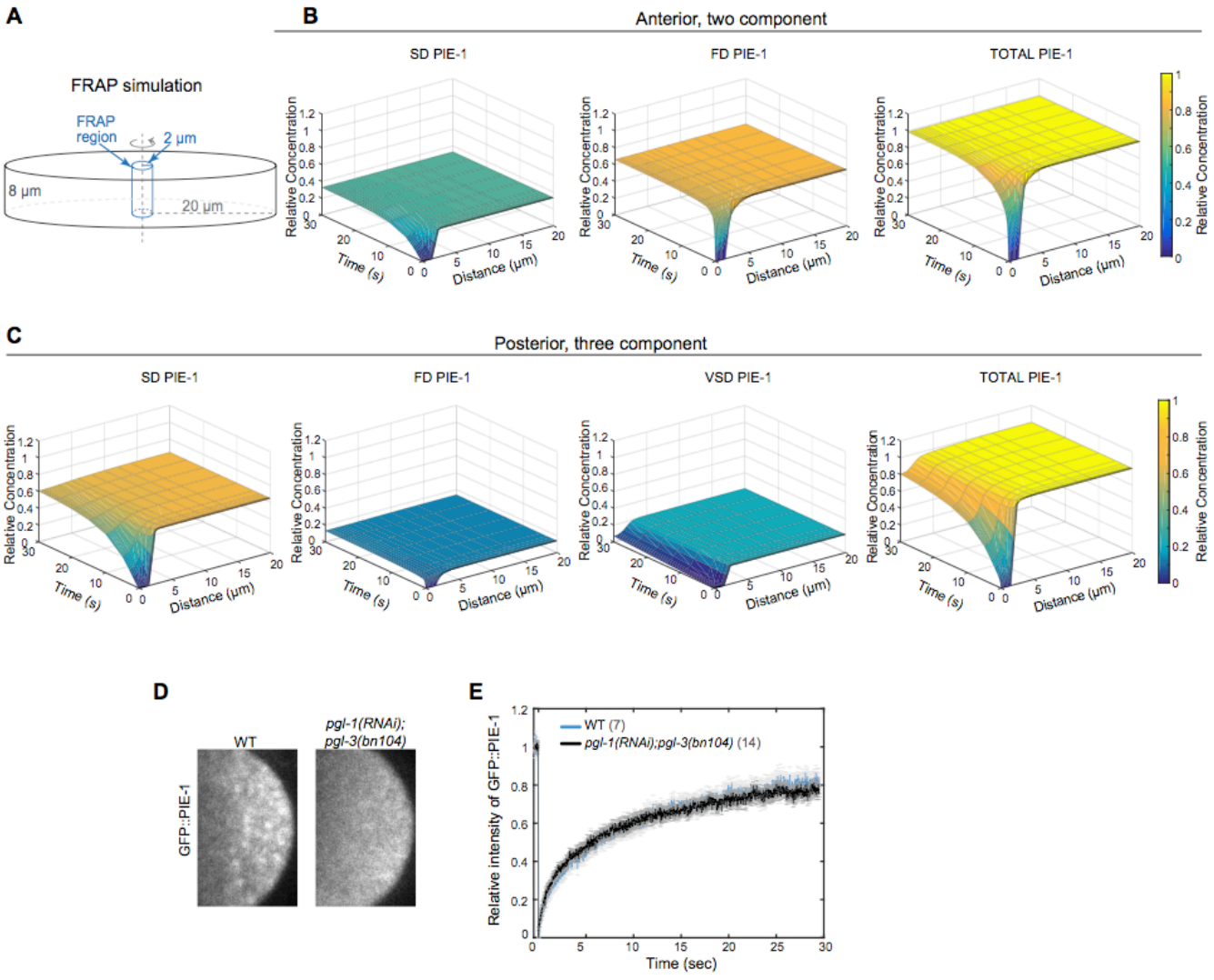

Fig. S5. FRAP simulation of PIE-1 and FRAP analysis of GFP::PIE-1 in *pgl-1(RNAi);pgl-3(bn104)* embryos. Related to Figures 4 and 5. **A.** Geometry of the FRAP simulation. FRAP simulation was performed with a cylindrical FRAP region with 2 µm radius (blue) in a cylindrical domain with 20 µm radius (black). **B.** Two component FRAP simulation of PIE-1 in the anterior. The concentration along the radius of the simulation domain is plotted. **C.** Three component FRAP simulation of PIE-1 in the posterior. The concentration along the radius of the simulation domain is plotted. Note that the FRAP simulation plots in Figures 4 and 5 are of the mean concentration within the FRAP region. **D.** Average projection of the first 20 frames of an example FRAP movie (before bleaching) for GFP::PIE-1 in the posterior domain. Note that GFP::PIE-1 association with P granules is significantly reduced in *pgl-1(RNAi);pgl-3(bn104)* embyros. **E.** FRAP analysis of GFP::PIE-1 in the posterior cytoplasm of wild-type embryos and *pgl-1(RNAi);pgl-3(bn104)* embryos.

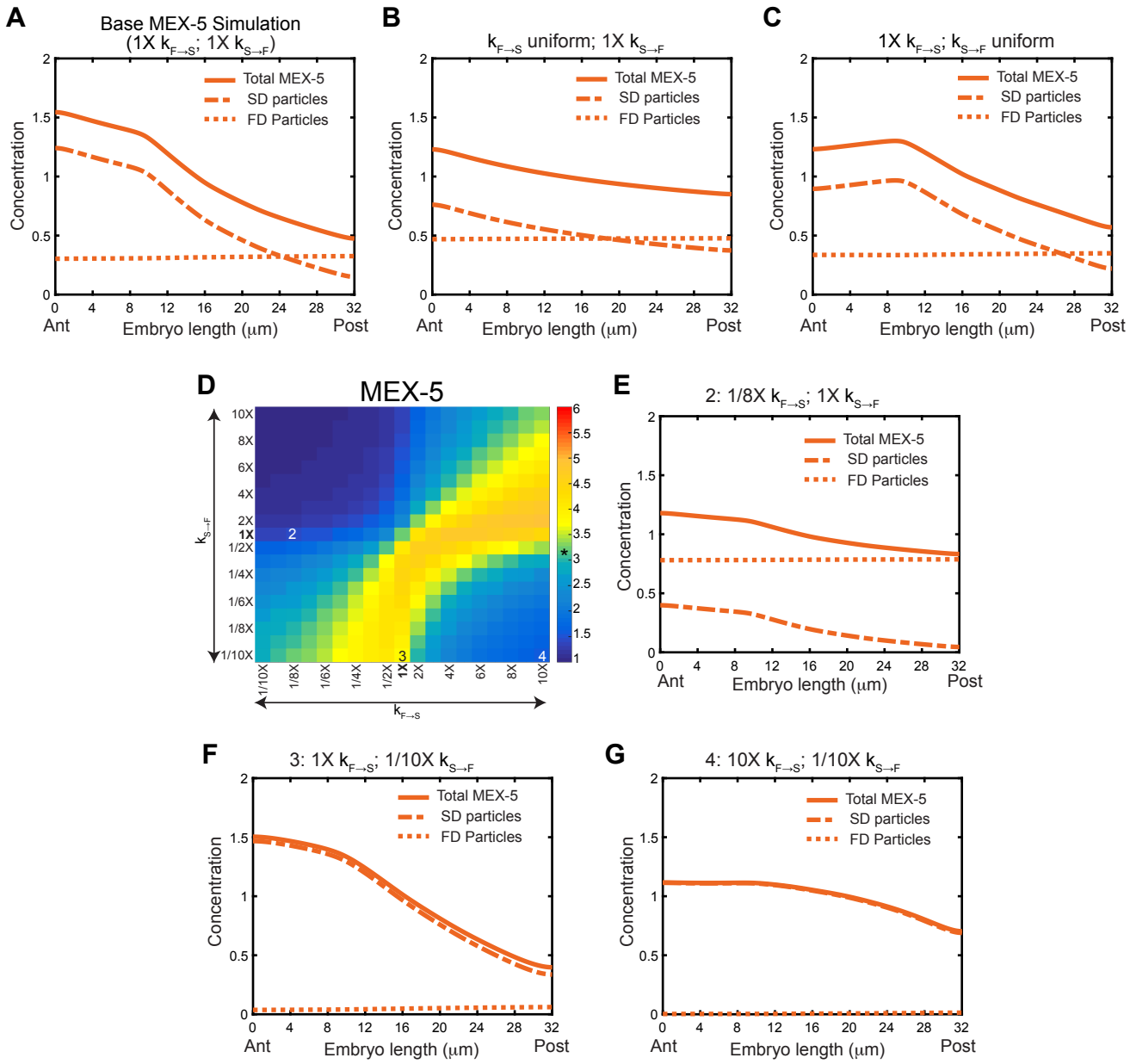

Fig. S6. Sensitivity of the MEX-5 simulation to changes in $k_{F\to S}$ and $k_{S\to F}$. Related to Figure 4. **A.** The base MEX-5 simulation at steady state, duplicated from Figure 4C. **B.** Concentration gradient when $k_{F\to S}$ is uniform. **C.** Concentration gradient when $k_{S\to F}$ is uniform. The majority of the differences in MEX-5 concentration are due to differences in $k_{F\to S}$ along the A/P axis. **D.** Duplicated from Figure 4O. **E-G.** The gradient of FD, SD and total protein corresponding to the labeled positions in D. **E.** Decreasing $k_{F\to S}$ alone decreases gradient amplitude. **F.** Decreasing $k_{S\to F}$ alone increases gradient amplitude. **G.** When $k_{F\to S} >> k_{S\to F}$, a very weak gradient forms because essentially all particles in the anterior and posterior cytoplasm are in the SD state.

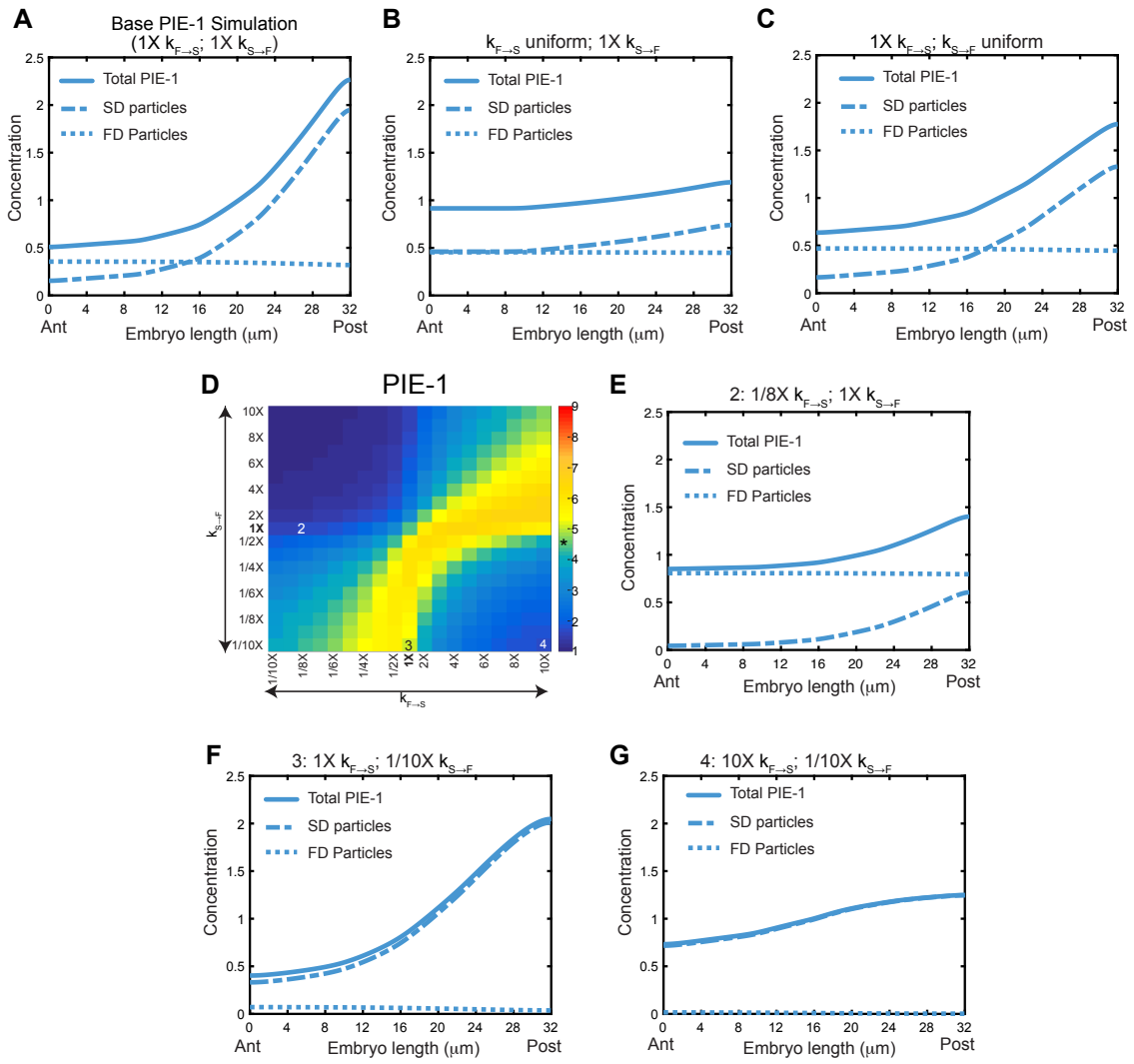

Fig. S7. Sensitivity of the PIE-1 simulation to changes in $k_{F\rightarrow S}$ and $k_{S\rightarrow F}$. Related to Figure 5. **A-C.** Individual contribution of $k_{F\rightarrow S}$ and $k_{S\rightarrow F}$ to PIE-1 concentration gradient. **A.** Duplicated from Figure 5C. **B.** Concentration gradient when $k_{F\rightarrow S}$ is uniform. **C.** Concentration gradient when $k_{S\rightarrow F}$ is uniform. Differences in $k_{F\rightarrow S}$ along the A/P axis can account for the majority of PIE-1 concentration gradient. **D-G.** The sensitivity of PIE-1 simulation to changes in $k_{F\rightarrow S}$ and $k_{S\rightarrow F}$. **D.** Duplicated from Figure 5K. **E-G.** The gradient of FD, SD and total protein corresponding to the labeled positions in D.

Supplemental Movie Legends

Movie S1. Near-TIRF imaging of GFP::MEX-5 at ~55 frames/second (18 msec exposures). 250 frames from a 2000-frame movie played at 1X speed. In all movies, anterior is to the left and posterior is to the right.

Movie S2. Near-TIRF imaging of GFP::PIE-1 at ~55 frames/second (18 msec exposures). 250 frames from a 2000-frame movie played at 1X speed.

Movie S3. Near-TIRF imaging of GFP::POS-1 at ~55 frames/second (18 msec exposures). 250 frames from a 2000-frame movie played at 1X speed.

Movie S4. Near-TIRF imaging of GFP::MEX-5 at ~20 frames/second (50 msec exposures). 250 frames from a 2000-frame movie played at 1X speed. Note that for Supplemental Movies S4 – S16, images were collected at relatively slow acquisition rates in order to blur the fast-diffusing particles, which facilitates analysis of the slow-diffusing particles by single particle detection and tracking. The same wild-type embryo is in Figure 1F and Figure 2A.

Movie S5. Near-TIRF imaging of GFP::PIE-1 at ~20 frames/second (50 msec exposures). 250 frames from a 2000-frame movie played at 1X speed. The same wild-type embryo is in Figure 1G and Figure 3A.

Movie S6. Near-TIRF imaging of GFP::MEX-5 in a *par-1 (RNAi)* embryo at ~20 frames/second (50 msec exposures). 250 frames from a 2000-frame movie played at 1X speed. The same embryo is in Figure S1G and Figure 2B.

Movie S7. Near-TIRF imaging of GFP::MEX-5 in a *pkc-3 (RNAi)* embryo at ~20 frames/second (50 msec exposures). 250 frames from a 2000-frame movie played at 1X speed. The same embryo is in Figure S1G.

Movie S8. Near-TIRF imaging of GFP::PIE-1 in a *mex-5/6 (RNAi)* embryo at ~20 frames/second (50 msec exposures). 250 frames from a 2000-frame movie played at 1X speed. The same embryo is in Figure S1H and Figure 3B.

Movie S9. Near-TIRF imaging of GFP::PIE-1 in a *par-1 (RNAi)* embryo at ~20 frames/second (50 msec exposures). 250 frames from a 2000-frame movie played at 1X speed. The same embryo is in Figure S1H.

Movie S10. A smPReSS movie of GFP::MEX-5 in a wild-type embryo. The first five frames and the last five frames were taken at 5-second intervals but are played at 10x speed. The rest of the movie is played at 1X speed. After the initial 5 frames, embryos were imaged continuously followed by a 45 second no-laser period to allow recovery. All images were collected with 50 msec exposures.

Movie S11. A smPReSS movie of GFP::MEX-5 in a *par-1(RNAi)* embryo. The movie was generated in the same manner as Movie S10.

Movie S12. A smPReSS movie of GFP::MEX-5 in a *pkc-3(RNAi)* embryo. The movie was generated in the same manner as Movie S10.

Movie S13. A smPReSS movie of GFP::MEX-5(ZFmut). The movie was generated in the same manner as Movie S10.

Movie S14. A smPReSS movie of GFP::PIE-1 in a wild-type embryo. The movie was generated in the same manner as Movie S10.

Movie S15. A smPReSS movie of GFP::PIE-1 in a *mex-5/6(RNAi)* embryo. The movie was generated in the same manner as Movie S10.

Movie S16. A smPReSS movie of GFP::PIE-1 in a *par-1(RNAi)* embryo. The movie was generated in the same manner as Movie S10.

References

1. Brenner S (1974) The genetics of *Caenorhabditis elegans*. *Genetics* 77:71-94.
2. Merritt C, et al. (2008) 3' UTRs are the primary regulators of gene expression in the *C. elegans* germline. *Curr Biol* 18:1476-1482.
3. Gallo CM, et al. (2010) Cytoplasmic partitioning of P granule components is not required to specify the germline in *C. elegans*. *Science* 330:1685-1689.
4. Tse YC, et al. (2012) RhoA activation during polarization and cytokinesis of the early *Caenorhabditis elegans* embryo is differentially dependent on NOP-1 and CYK-4. *Mol Biol Cell* 23:4020-4031.
5. Han B, Antkowiak KR, Fan X, Rutigliano M, Ryder SP, Griffin EE (2018) Polo-like kinase couples cytoplasmic protein gradients in the *C. elegans* zygote. *Curr Biol* 28:60-69.
6. Timmons L, Fire A (1998) Specific interference by ingested dsRNA. *Nature* 395:854.
7. Arribere JA, et al. (2014) Efficient marker-free recovery of custom genetic modifications with CRISPR/Cas9 in *Caenorhabditis elegans*. *Genetics* 198:837-846.
8. Paix A, et al. (2015) High efficiency, homology-directed genome editing in *Caenorhabditis elegans* using CRISPR-Cas9 ribonucleoprotein complexes. *Genetics* 201:47-54.
9. Robin FB, et al. (2014) Single-molecule analysis of cell surface dynamics in *Caenorhabditis elegans* embryos. *Nat Methods* 11:677-682.
10. Sailer A, et al. (2015) Dynamic opposition of clustered proteins stabilizes cortical polarity in the *C. elegans* zygote. *Dev Cell* 35:131-142.
11. Crocker JC, Grier DG (1996) Methods of digital video microscopy for colloidal studies. *J Colloid Interf Sci* 179:298-310.
12. Jaqaman K, et al. (2008) Robust single-particle tracking in live-cell time-lapse sequences. *Nat Methods* 5:695-702.
13. Griffin EE, Odde DJ, Seydoux G (2011) Regulation of the MEX-5 gradient by a spatially segregated kinase/phosphatase cycle. *Cell* 146:955-968.